Large-amplitude gravity waves above the southern Andes, the Drake Passage, and the Antarctic Peninsula

A. de la Torre,[1] P. Alexander,[2] R. Hierro,[1] P. Llamedo,[1] A. Rolla,[1] T. Schmidt,[3] and J. Wickert[3]

Received 8 June 2011; revised 17 November 2011; accepted 17 November 2011; published 24 January 2012.

[1] Above the southern Andes range and its prolongation in the Antarctic Peninsula, large-amplitude mountain and shear gravity waves observed with Weather Research and Forecasting (WRF) mesoscale model simulations during winter 2009 are analyzed. Two specific reasons motivated this study: (1) a decade of satellite observations of temperature fluctuations in the stratosphere, allowing us to infer that this region may be launching the largest-amplitude gravity waves into the upper atmosphere, and (2) the recent design of a research program to investigate these features in detail, the Southern Andes Antarctic Gravity wave Initiative (SAANGRIA). The simulations are forced with ERA-Interim data from the European Centre for Medium-Range Weather Forecasts. The approach selected for the regional downscaling is based on consecutive integrations with weekly reinitialization with 24 h of spin-up, and the outputs during this period are excluded from the analysis. From 1 June to 31 August 2009, five case studies were selected on the basis of their outstanding characteristics and large wave amplitudes. In general, one or two prevailing modes of oscillation are identified after applying continuous wavelet transforms at constant pressure levels and perpendicularly to the nominal orientation of the dominant wave crests. In all cases, the dominant modes are characterized by horizontal wavelengths around 50 km. Their vertical wavelengths, depending on a usually strong background wind shear, are estimated to be between 2 and 11 km. The corresponding intrinsic periods range between 10 and 140 min. In general, the estimated vertical wavelength (intrinsic period) maximizes (minimizes) around 250–300 hPa. The synoptic circulation for each case is described. Zonal and meridional components of the vertical flux of horizontal momentum are shown in detail for each case, including possible horizontal wavelengths between 12 and 400 km. Large values of this flux are observed at higher pressure levels, decreasing with increasing height after a progressive deposition of momentum by different mechanisms. As expected, in the wintertime upper troposphere and lower stratosphere in this region, a prevailing zonal component is negative almost everywhere, with the exception of one case above the northern tip of the Antarctic Peninsula. A comparison with previous experimental results reported in the region from in situ and remote sensing measurements suggests a good agreement with the momentum flux profiles computed from the simulations. Partial wave reflection near the tropopause was found, as considerable departures from equipartition between potential and kinetic wave energy are obtained in all cases and at all pressure levels. This ratio was always less than 1 below the lower stratosphere.

Citation: de la Torre, A., P. Alexander, R. Hierro, P. Llamedo, A. Rolla, T. Schmidt, and J. Wickert (2012), Large-amplitude gravity waves above the southern Andes, the Drake Passage, and the Antarctic Peninsula, *J. Geophys. Res.*, *117*, D02106, doi:10.1029/2011JD016377.

1. Introduction

[2] Internal gravity waves (GWs) play a very important role in many dynamic and plasma processes extending from the Earth's surface upward into the thermosphere and ionosphere. They are major contributors to the atmospheric structure and produce effects that impact the atmosphere at essentially all altitudes and all spatial and temporal scales. The main GW sources are found in the troposphere and lower stratosphere [e.g., *Fritts and Alexander*, 2003]. In

[1]Facultad de Ingeniería, Universidad Austral, Buenos Aires, Argentina.
[2]Departamento de Física, Facultad de Ciencias Exactas y Naturales, Universidad de Buenos Aires, Buenos Aires, Argentina.
[3]Helmholtz Centre Potsdam, GFZ German Research Centre for Geosciences, Potsdam, Germany.

0148-0227/12/2011JD016377

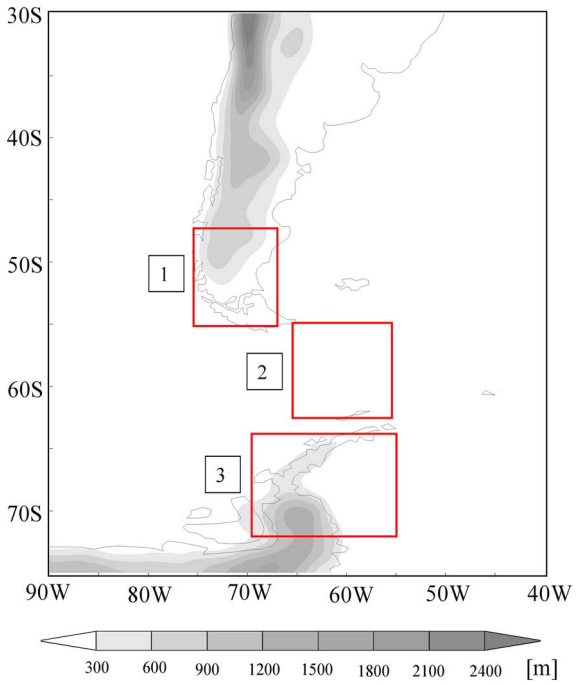

Figure 1. The three considered regions for the numerical simulations.

general circulation models, GWs drag has been usually treated with parameterizations. These models, because of their spatial and temporal resolutions, cannot explicitly resolve subgrid GWs phenomena like GWs drag. A primary limitation in development and validation of these representations has been the lack of observational constraints on waves. Moreover, it is very difficult to obtain a complete view of three-dimensional time-varying atmospheric processes with a single instrument or technique [*Wu et al.*, 2006]. Radiosonde, lidar, radar, and rocket measurements generally provide local observations of GWs, whereas measurements on board satellites can yield global coverage. Nevertheless, our understanding of GW dynamics and their effects remains limited in important areas.

[3] In particular, GWs generated by flow over mountains have strong impact on mesoscale circulation, precipitation and turbulence occurrence and intensity. Large terrain features such as mountain ranges create mountain waves (MW) that transport energy and mean flow horizontal momentum away from the lower atmosphere toward the middle and upper atmosphere, where they are deposited. It is now recognized that this deposition of energy and momentum is an essential component of global circulation. Short and mesoscale GWs significantly contribute to the momentum balance of the stratosphere [e.g., *Fritts and Alexander*, 2003].

[4] Horizontal momentum is transported by MWs from the region of wave dissipation to the surface, where a net pressure force is exerted by Newton's third law on the topography. A decelerative force is exerted on the large scale atmospheric circulation in those regions where the wave undergoes dissipation. The basic structure of a MW is determined by the size and shape of the mountains, by the vertical profiles and lapse rates of temperature (T), wind speed and moisture in the impinging flow [e.g., *Gill*, 1982]. Nonlinear effects exert a significant influence on the wave amplitude and are essential to the dynamics of MW dissipation in regions of wave breaking by overturning. As is known, the largest momentum fluxes are carried by those waves with short horizontal (λ_H) and long vertical wavelengths (λ_z) [e.g., *Preusse et al.*, 2008]. The deposition of momentum (sometimes called drag or stress) on the atmosphere has deep and profound and important effects on all scales of flow. For example, the quasi-biennial and semiannual oscillations in equatorial zonal winds are at least partially driven by the convergence of momentum carried by GWs [e.g., *Ern et al.*, 2004, and references therein]. An early direct observation of momentum (in the mesosphere) by GWs was made by *Vincent and Reid* [1983] using a split beam technique with an HF radar.

[5] We now know that during winter, the region close to the southern Andes, the Drake Passage and the Antarctic Peninsula is one of the most energetic regions on Earth for the deep vertical propagation of GWs. It presents one of the largest, if not the largest, mesoscale (10 to 1000 km) variability at altitudes from 20 to 60 km of any region on Earth [e.g., *Plougonven et al.*, 2008; *Shutts and Vosper*, 2011]. In situ measurements with superpressure balloons were obtained in 2005 in the late winter and early spring polar vortex of the Southern Hemisphere [*Vincent et al.*, 2007]. The balloons could drift for months in the stratosphere acting as quasi-Lagrangian tracers of air-parcel motions. The importance of mountain waves in the Southern Hemisphere was confirmed, with largest momentum fluxes observed in the lee of the Antarctic Peninsula. However, significant momentum fluxes were also observed over the ocean. The magnitude of the fluxes have mean values of 3.4 mPa. The zonal momentum flux is negative almost everywhere, which indicates that the vast majority of GW are propagating against the mean eastward flow characteristic of the wintertime stratosphere. The largest westward fluxes are found above or in the lee of major orography, and locally reach 12 mPa over the Antarctic Peninsula. Much stronger individual wave packets that had fluxes 50 times larger than the average were locally observed directly above the Peninsula. Orographic waves carried about 2/3 of the total momentum flux above Antarctica. From 27 long-duration balloons between September 2005 and February 2006 over Antarctica and the Southern Ocean, *Boccara et al.* [2008] and *Hertzog et al.* [2008] studied the geographic variability of GW momentum flux in the lower stratosphere. The largest time-averaged value (28 mPa) was observed above the Antarctic Peninsula. This value exceeds by a factor about 10 the overall mean momentum flux measured during the balloon campaign. Because of its steep orography and of its roughly north-south orientation, the Antarctic Peninsula was confirmed as a very active area for the generation of GWs and likely to have a profound impact on the dynamics of the Southern Hemisphere polar stratosphere. Zonal momentum fluxes were predominantly westward. When zonal averages were performed, oceanic momentum fluxes were found to be of similar magnitude to continental values (2.5–3 mPa), showing the importance of nonorographic gravity waves over oceans. They appeared to be significantly more sporadic than waves observed above the ocean. The magnitude of momentum flux was found to be larger at the beginning of the campaign (September–October) than at the end of it

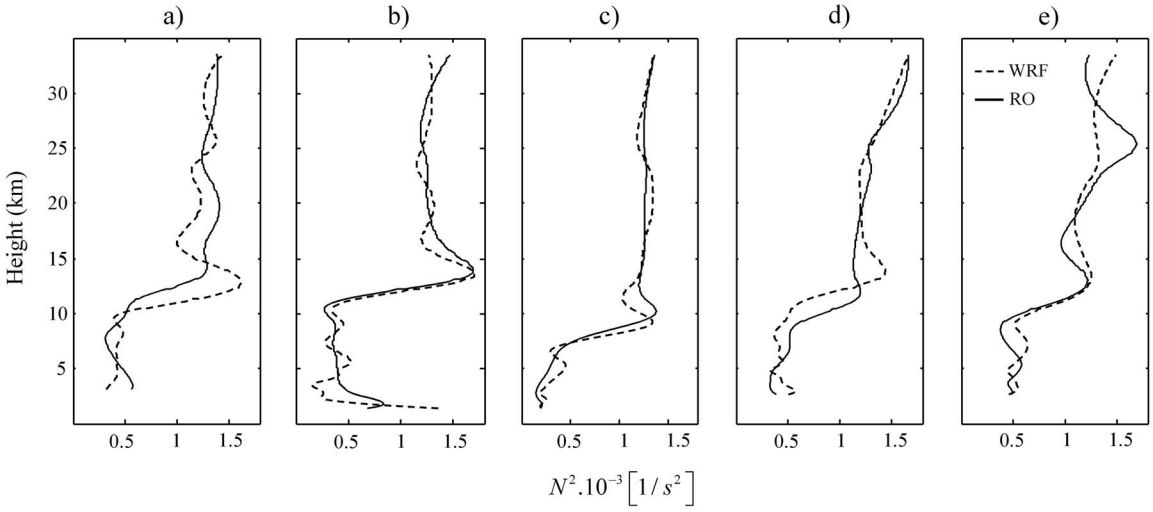

Figure 2. Squared buoyancy frequency computed from *T* radio occultation (RO) profiles, retrieved from Constellation Observing System for Meteorology, Ionosphere, and Climate (COSMIC) and from Weather Research and Forecasting (WRF) simulations, corresponding to case (a) 1, (b) 2, (c) 3, (d) 4, and (e) 5. Time and average position of the five RO events are (1) 16 July 08:00 UT, 51.65°S, 73.96°W, (2) 25 June 18:00 UT, 53.11°S, 74.45°W, (3) 21 June 09:00 UT, 55.41°S, 64.87°W, (4) 28 July 19:00 UT, 68.64°S, 67.65°W, and (5) 19 July 12:00 UT, 67.27°S, 65.04°W.

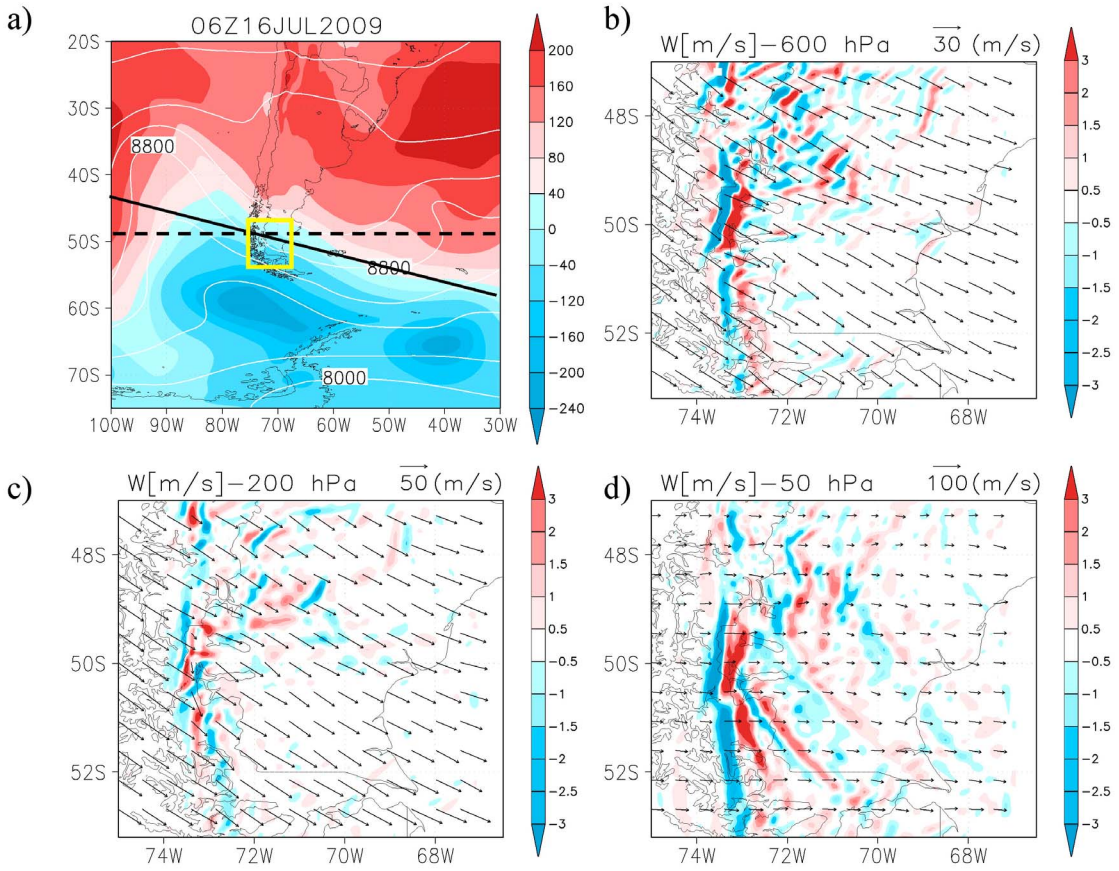

Figure 3. Case 1: (a) 1000 and 200 hPa geopotential height (shaded regions and white curves, respectively). Black lines represent the proposed racetrack (solid line) and dominant GW propagation direction (dashed line). Also shown are *u* and *w* at (b) 600, (c) 200, and (d) 50 hPa levels. The yellow bounding box in Figure 3a presents the outer bounds of Figures 3b–3d.

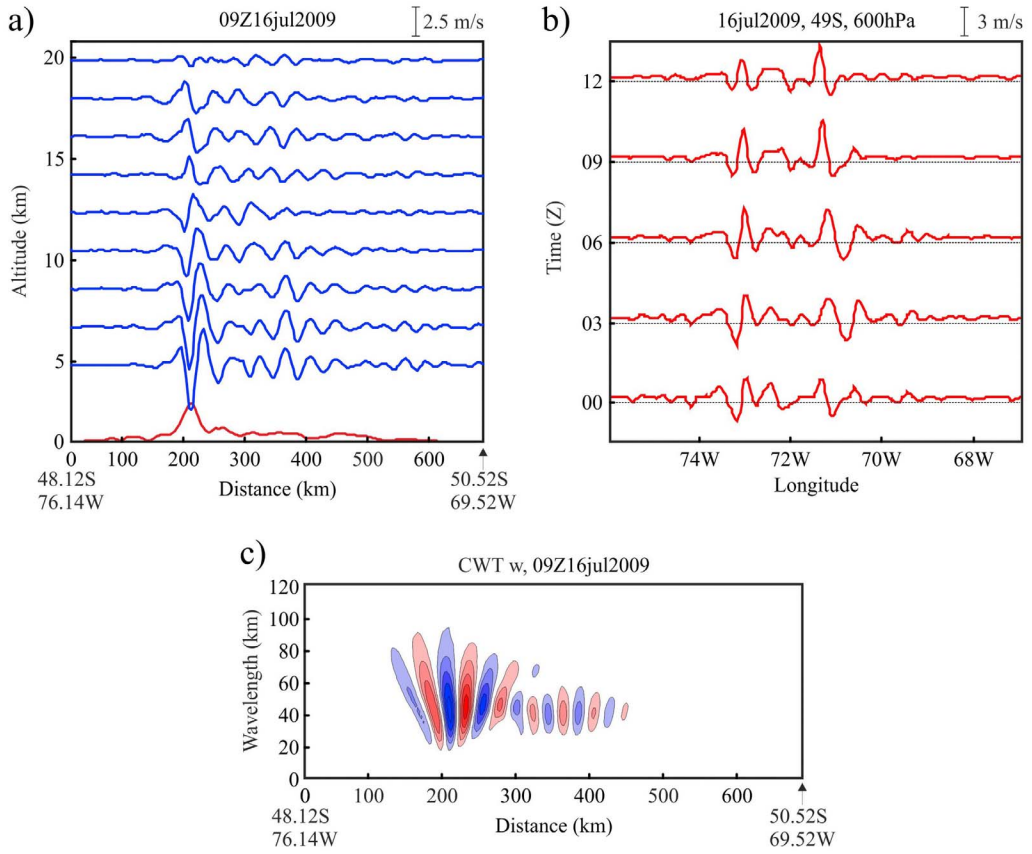

Figure 4. Case 1: *w* as a function of (a) altitude along the perpendicular direction to the dominant wave crests shown in Figure 3a and (b) time along the proposed racetrack direction (Figure 3a). (c) The *w* continuous wavelet transform (CWT) at 600 hPa along the same direction as in Figure 4a. The bottom red contour in Figure 4a represents the topographic level.

(December–January). *Plougonven et al.* [2008] obtained momentum flux results during spring above the Antarctica Peninsula, corresponding to a large-amplitude mountain wave breaking there. Mesoscale numerical simulations and measurements from superpressure balloons were obtained. Local values of momentum flux, averaged over boxes 140 km × 140 km, reached 7 to 9 Pa at heights between 15 and 20 km.

[6] In the last 15 years, remote sensing measurements from limb scanning satellite data allowed to derive *T* vertical profiles. These provide a low level limit to momentum flux, under specific theoretical constraints [see, e.g., *Ern et al.*, 2004]. A critical point here consists in the accurate determination of the horizontal component of the wave number vector associated to the prevailing GW mode that effectively contributes to the momentum flux. From Cryogenic Infrared Spectrometers and Telescopes for the Atmosphere (CRISTA) data during August 1997 and at 25 km height, momentum flux values between 2.5 and 25 mPa were found. More recently, from High Resolution Dynamics Limb Sounder (HIRDLS) data, *Alexander et al.* [2008] obtained global estimates of momentum flux, averaged between 20 and 30 km height for 16 May 2006, reporting values between 2.5 and 5 mPa in the southern tip of the Andes Range. *T* soundings from the Constellation Observing System for Meteorology, Ionosphere, and Climate (COSMIC) and Challenging Minisatellite Payload (CHAMP) global positioning system radio occultation (GPS RO) missions were used to derive momentum flux in the altitude range of 17.5 and 22.5 km from December 2006 to February 2007 [*Wang and Alexander*, 2010]. Similar values to those reported in previous studies in the region considered by *Ern et al.* [2004] and *Alexander et al.* [2008] were obtained. From nadir scanning satellite *T* data with the Atmospheric Infrared Sounder (AIRS), an event of 140 mPa at 40 km height with λ_H = 300 km and λ_z = 20 km was detected [*Alexander and Teitelbaum*, 2007]. With this same instrument, events over southern Georgia were described by *Alexander et al.* [2009], including a range of λ_H between 50 and 400 km and averaged over a 2.5° latitude per 2.5° longitude area. Momentum fluxes ranging between 60 and 200 mPa were reported, with local values greater than 1000 mPa.

[7] This recent evidence of a considerable enhanced wave activity above the southern Andes, the Drake Passage and the Antarctic Peninsula justified the design of a new research program. It has been proposed to combine new measurements, spanning altitudes from the Earth's surface to the mesopause, with mesoscale models capable of describing GW dynamics and effects from turbulence to planetary scales [*Fritts et al.*, 2010]. The Southern Andes Antarctic Gravity wave Initiative (SAANGRIA) project includes a field measurement campaign planned from June to September 2013 to study the dynamics of GW in the

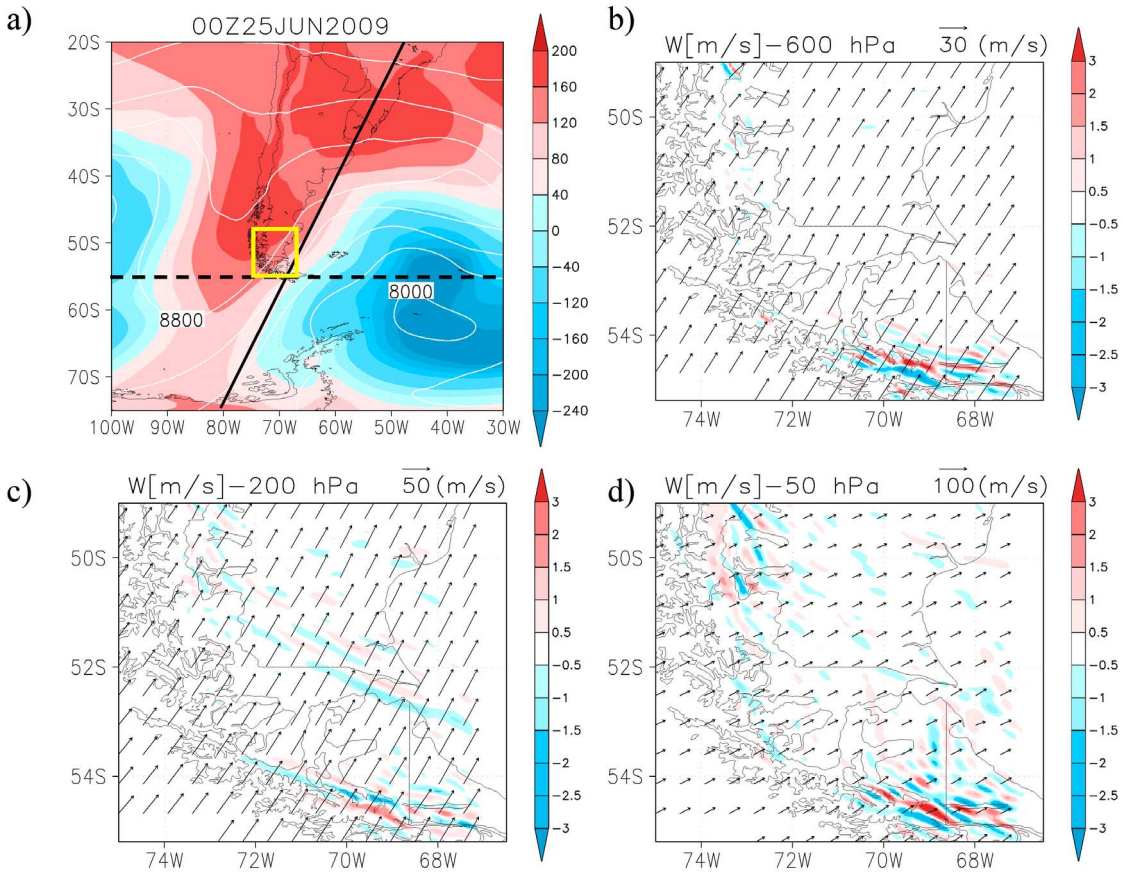

Figure 5. The same as Figure 3, but for case 2.

southern Andes–Antarctic Peninsula region, from the surface of the Earth to the mesosphere and lower thermosphere (MLT). The experiment will take place during winter, coinciding with the maximum in GW activity and its apparent influence in the stratosphere, mesosphere, and lower thermosphere. The main objectives of this project are (1) detailed measurements and modeling of GW dynamics, including their sources, propagation, instabilities, and effects, (2) analysis of GW variations with altitude, (3) propagation, filtering, and nonlinear interaction studies addressing GW (mainly MW) penetration into the MLT, and (4) predictability studies of MWs and GWs for numerical weather prediction, climate, and general circulation models. The observational evidence of anomalous high wave activity in this region and the consequent design of the SAANGRIA Experiment motivated the present study. In section 2, we describe the numerical simulations and their validation through experimental GPS radio occultation data; section 3 describes the wave analysis to be performed for each of the five cases considered; in section 4, the calculation of momentum flux as well as the ratio between potential and kinetic wave energy is discussed and in section 5 some conclusions are outlined.

2. Numerical Simulations

[8] In five representative examples taken during winter 2009, we describe simulations using the Weather Research and Forecasting (WRF 3.0) regional model [*Skamarock et al.*, 2008]. The regional circulation and the vertical (w), zonal (u) and meridional (v) velocity and T fields before and during the development of these events were determined. The simulations were forced with ERA-Interim data with a resolution of 0.5° × 0.5° [*Simmons et al.*, 2007] to construct initial and boundary conditions. The approach selected for the regional downscaling was consecutive integrations with weekly reinitialization with 24 h of spin-up and the outputs during this period were excluded from the analysis. Each reinitialization run for 8 days whose total integration time spans the integration periods selected [*von Storch et al.*, 2000]. They were carried out in three different regions of interest (Figure 1) with 60 vertical levels, 2.75 km meridional resolution and a zonal resolution ranging from 2 km (at 47°S) to 1.0 km (at 72°S). Synoptic conditions were obtained from global ERA-Interim data fields. The dates selected from June, July and August 2009 correspond to cases 1–5 below (16 July, 25 June, 21 June, 28 July, and 19 July, respectively). Each date was selected because of its outstanding wave amplitude. We describe from w the wave structure observed as a function of height along vertical cross sections perpendicularly to the nominal orientation of the dominant wave crests corresponding to each case. In particular, we also show w variability at 600 hPa and constant latitude to verify the stationary or nonstationary character. Additionally, we intended to observe typical structures that may be picked up by an aircraft along different

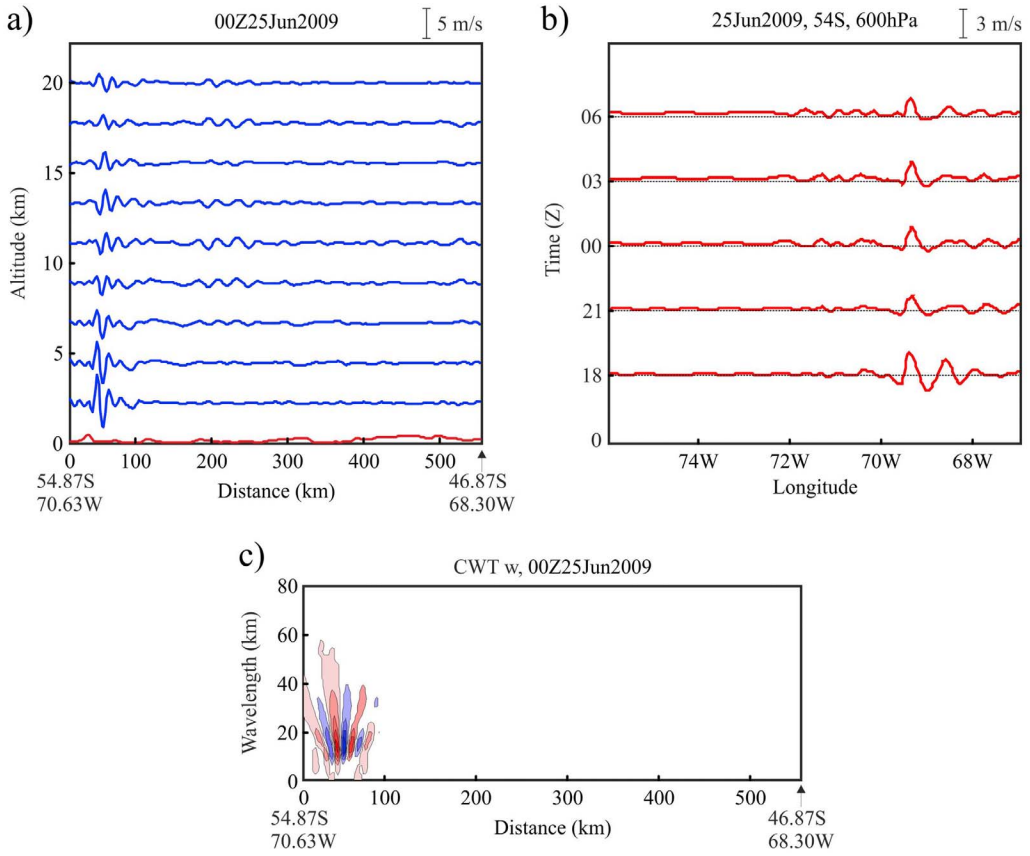

Figure 6. Case 2: w as a function of (a) altitude along the perpendicular direction to the dominant wave crests shown in Figure 5a and (b) time along the proposed racetrack direction (Figure 5a). (c) The w CWT at 600 hPa along the same direction as in Figure 6a.

racetracks, for future comparison with SAANGRIA experimental data. These racetracks, proposed above the mountain tops and the Drake Passage, roughly correspond to latitudes 49°, 54°, 59°, 65°, and 71°S (in coincidence with cases 1–5 below, respectively). It is generally accepted that w constitutes an appropriate dynamical variable to establish the presence of MWs [e.g., *Smith*, 1979; *Shutts et al.*, 1988].

[9] To validate the simulations, the buoyancy frequency N was computed from available T GPS-COSMIC radio occultation (RO) profiles for the five cases considered (Figure 2). The individual data of each RO profile generate a so-called line of tangent points (LTP) (solid lines). The upper limit and ground level corresponding to each LTP are horizontally separated up to 100 km. This may result in an atmospheric sounded region quite different from the vertical direction. In Figure 2, dashed lines represent N^2 as a function of altitude derived from WRF T simulations, interpolated along the corresponding LTPs. In the 5 cases, 50 pairs of points are considered and the calculated linear correlation coefficient is always greater than 0.99. The probability that these high correlation coefficients may be a by-product of chance (hypothesis test performed) is lower than 0.0001.

3. Wave Analysis

[10] The 3-D nature of GW signatures allows us to perform the wave analysis along vertical, horizontal, or even slanted directions. In our case, because of the characteristics of the region under study, with expected dominant high and moderate intrinsic frequency modes, we analyzed the variability along vertical cross sections perpendicularly to the dominant wave crests and at fixed latitudes and standard tropospheric and stratospheric pressure levels. The horizontal resolution available at each domain is sufficient for typical λ_H longer than 15 km, according to dominant waves found in previous analyses in the region [e.g., *de la Torre et al.*, 2006]. To isolate dominant spectral components and to determine their horizontal direction of propagation, a Morlet continuous wavelet transform (CWT) was applied to w. A basic capability of a CWT analysis is the localization of main modes of oscillation in restricted intervals of the data series. These are expected to take place near the mountainous regions in cases 1, 2, 4, and 5. λ_H for each dominant mode is expected to be mostly preserved throughout the troposphere. Because of refraction effects and the intense background wind shear in the region, this is not the case for λ_z, in the numerical simulations ground referred inertial frame. To determine the predominant modes and the horizontal direction of propagation applying the CWT analysis, we first considered horizontal profiles (HP) at standard pressure levels in domains 1, 2, and 3, respectively. These were taken roughly perpendicular to the wave crests. A nonrecursive low-pass filter with a Kaiser window [e.g., *Hamming*, 1998] and a cutoff at 400 km is applied to each HP to remove the background. Subtracting filtered from not

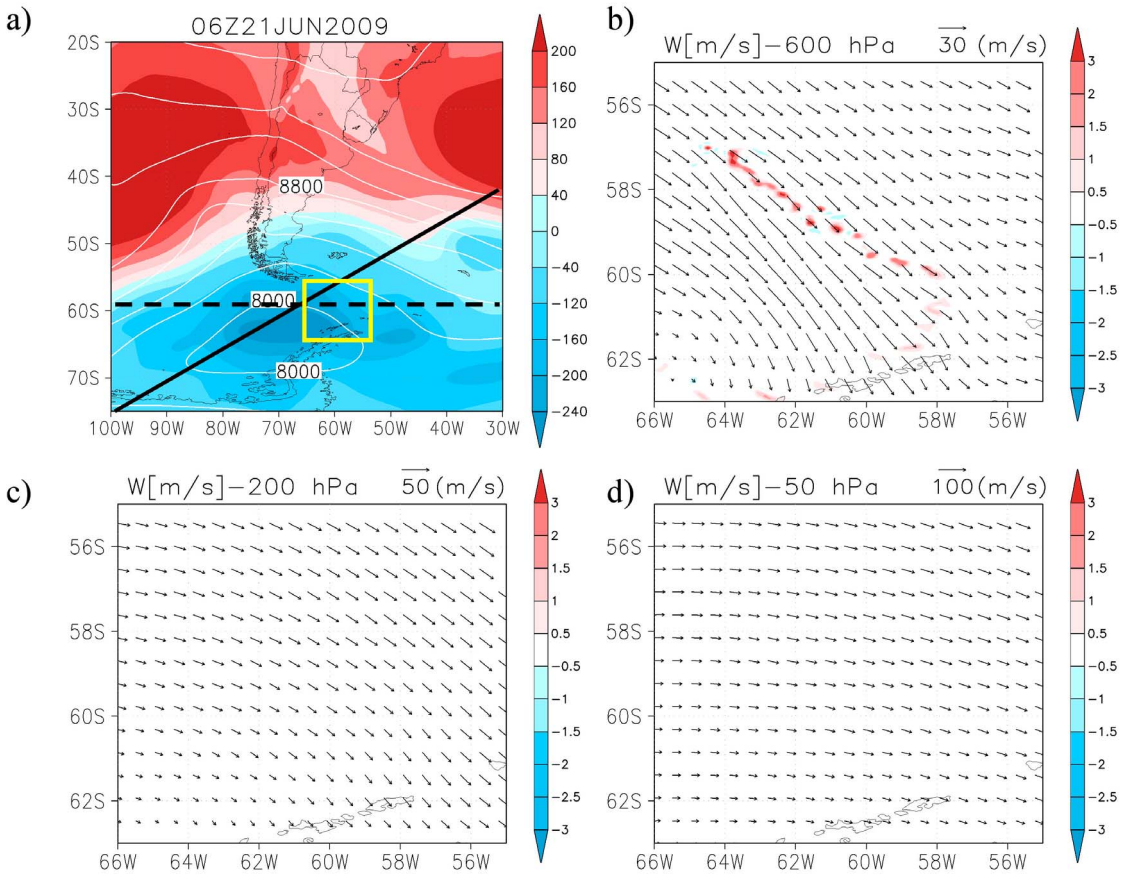

Figure 7. The same as Figure 3, but for case 3.

filtered HP, we obtain $w_{<400}$. The filter was applied again with cutoff at 12 km and aliasing effects are eliminated, thus obtaining each band-passed w_{bp} between 12 and 400 km (we omit the subindex $_{bp}$ below in all variables). Then, we observed the variation in CWT for slightly different directions around that roughly perpendicular to the wave crests (Figures 3a, 5a, 7a, 9a and 11a). The "actual" horizontal wave vector (k_H) direction of propagation should be that in which $k_H(\lambda_H)$ is maximum (minimum). This procedure allows the estimation of horizontal propagation directions from horizontal experimental or numerical data, in the presence of complex MW structures, as in cases 1 and 5 below. In more simple cases with bidimensional MW crests, like cases 2, 3, and 4, we proceeded considering CWTs corresponding to the zonal and meridional HPs for w. Then, after the identification of the dominant zonal and meridional wavelengths, the direction of k_H was determined.

3.1. Case 1 (16 July, 49°S)

3.1.1. Synoptic Circulation

[11] This event (Figure 3a) is characterized by a low-pressure system crossing the Drake Passage at 06:00 UT, while at the same time in the upper troposphere a long-wave trough is located over the Pacific Ocean, yielding a NW-SE circulation over Patagonia and most of the Drake Passage (Figure 3b). It can be seen that both the pressure system and the upper level trough are not in phase and show a west tilting with height. However, over Patagonia, both the low level flow and the upper level flow, present a NW-SE circulation because of the position of the NE region of the cyclone in the former and the long-wave trough in the latter. As a result, the component of rotation in wind shear does not seem to be important, keeping the same wind direction from low to upper level in the troposphere (Figures 3c and 3d).

3.1.2. Wave Parameters

[12] A large-amplitude, stationary structure forced by the mountains up to the stratosphere, persistent during at least 12 h, is observed (Figures 4a and 4b). A dominant mode (solid line in Figure 3a), with λ_H around 50 km (from the w CWT at 600 hPa) is shown in Figure 4c. Because of the strong vertical variability in the background wind, λ_z, calculated from

$$\lambda_z = 2\pi\left(\frac{N^2}{U_H^2} - k_H^2\right)^{0.5}, \qquad (1)$$

where U_H is the absolute value of the horizontal wind in the direction of $\mathbf{k}_H$, was estimated between 5 and 11 km. U_H ranges between 26 m/s and 49 m/s (this last at 250 hPa). The intrinsic period (τ) of this mode varies between 17 and 34 min. λ_z (τ is maximum (minimum) around 300 hPa. w peak-to-peak amplitudes reach maximum values near to 7 m/s at lower levels (600 hPa).

[13] Case 1 is much stronger than the other events shown. The second and next intense events are not presented here, as it was detected that they also belonged to the latitudes

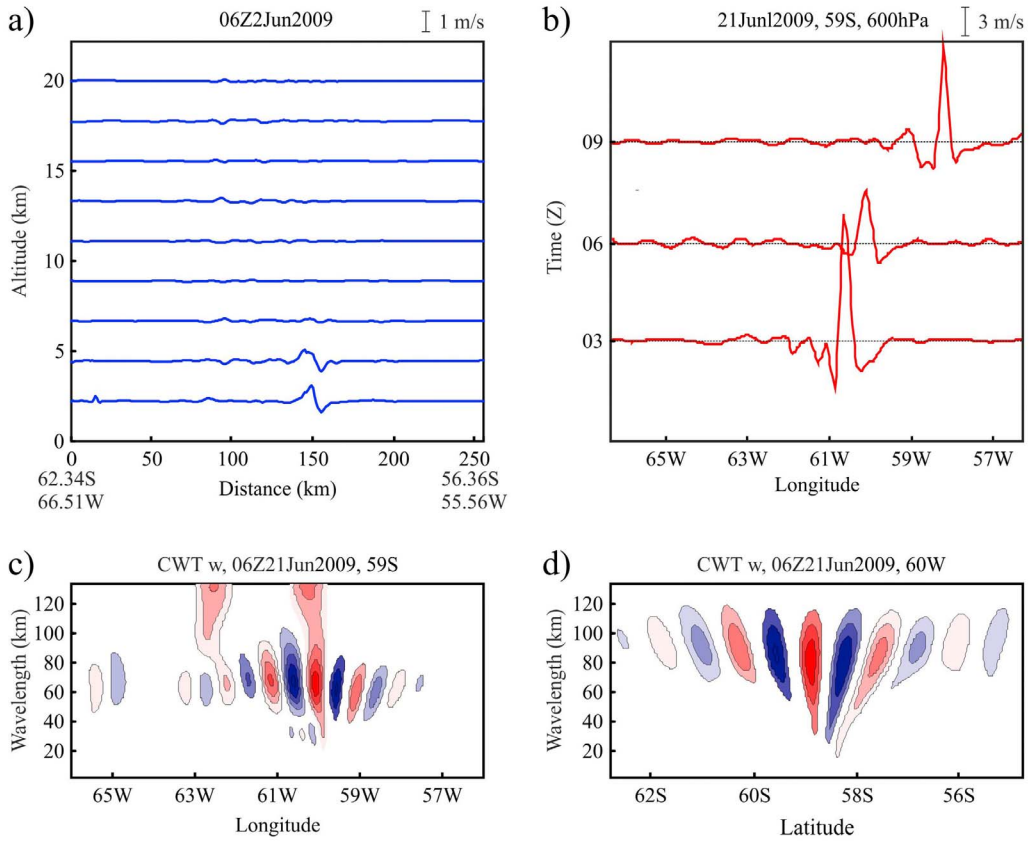

Figure 8. Case 3: w as a function of (a) altitude along the perpendicular direction to the dominant wave crests shown in Figure 7a and (b) time along the proposed racetrack direction (Figure 7a). The w CWT at 600 hPa along (c) the same direction as in Figure 8a and (d) perpendicular to it.

corresponding to case 1. Each of the five cases was selected because of its outstanding intensity in comparison to the remaining cases at that latitude during the study period. Nevertheless, we may assert that, for example at latitudes corresponding to cases 4 and 5 above the Antarctic Peninsula, additional intense events with similar amplitudes were systematically observed whenever similar horizontal mean flow directions took place in these regions.

3.2. Case 2 (25 June, 54°S)

3.2.1. Synoptic Circulation

[14] In this case (Figure 5a), an anticyclonic flow near the surface is present over the whole continental zone, while a large-amplitude ridge is observed in the upper troposphere. Over the Drake Passage, a transition region between a cyclonic circulation to the east and the mentioned anticyclone over the west at low levels is present. As a result, it is possible to distinguish a low level and an upper level flow entering the continent from SW (Figures 5a–5d).

3.2.2. Wave Parameters

[15] This flow forces large-amplitude stationary MWs with w peak-to- peak amplitudes ranging between 1.6 and 2.0 m/s at all levels, close to the southern tip of the Andes Range (Figures 6a and 6b). A predominant mode (solid line in Figure 5a) propagating against the mean wind, with λ_H around 18 km (from the w CWT at 600 hPa), is shown in Figure 6c. λ_z was estimated between 5.0 and 9.5 km. U_H ranges between 12 and 45 m/s (this last at 250 hPa). τ for this mode varies between 10 and 17 min. λ_z (τ) is maximum (minimum) around 250 hPa.

3.3. Case 3 (21 June, 59°S)

3.3.1. Synoptic Circulation

[16] A low level pressure system is located over the south of Argentina, with its center over the Drake Passage (Figure 7a). In the upper troposphere, a long-wave trough with its axis over the continent is in phase with this low-pressure system, suggesting that this case is a barotropic cyclone. As a result, the wind field does not show strong variations, either in intensity or rotation, between the lower and upper levels of the troposphere. Both the lower and upper level associated circulations present a NW-SE flow (Figures 7b–7d). This is the most significant case detected above the Drake Passage during winter 2009. MWs are not observed in this region.

3.3.2. Wave Parameters

[17] A linear structure (Figure 7b) of nonstationary (Figures 8b) GWs at 600 hPa from NW to SE is observed. In this case, the direction of propagation (solid line in Figure 7a) was determined from w CWTs using constant latitude (59° S) and longitude (61°W) HPs, respectively, with an intersection at 59°S, 61°W. The zonal and meridional wavelength components of the predominant mode yielded 60 and 80 km, respectively (Figures 8c and 8d). This corresponds to a SW-NE direction of propagation at 37° from the zonal direction. The westward progression of the wave packet

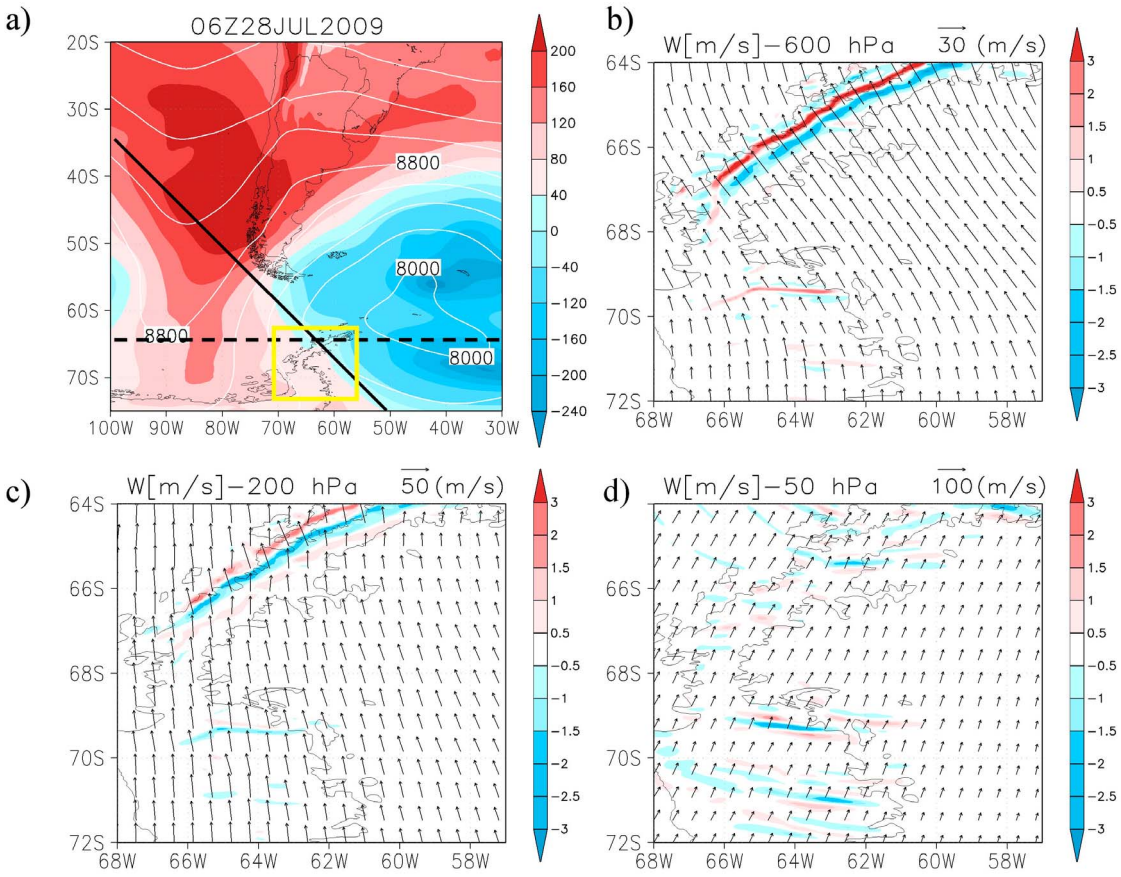

Figure 9. The same as Figure 3, but for case 4.

may be inferred from Figure 8b. Nevertheless, another direction of propagation at −37° would be possible from *w* CWT results too. This possibility is discarded, given the negative signs in both zonal and meridional components of the vertical flux of horizontal momentum. The ratio between these components may be, considered, under certain hypothesis, to be proportional to the ratio between zonal and meridional wave number components [*Ern et al.*, 2004] (see Figure 13c in section 4). U_H ranges between 18 and 30 m/s (this last at 50 hPa). *w* peak-to-peak amplitudes present maximum values near to 2.5 m/s at lower levels (600 hPa) and decrease with increasing height. The potential temperature vertical profile (not shown) suggests the breaking of this wave around 300 hPa, in agreement with the abrupt cancellation of momentum flux (as seen in Figure 13c). The generation of this wave by a shear mechanism at low levels may explain these structures.

3.4. Case 4 (28 July, 65°S)

3.4.1. Synoptic Circulation

[18] The South Pacific subtropical anticyclone penetrates the continent from the south, while a low-pressure system leaves the Drake Passage during its eastward displacement (Figure 9a). The upper level field is in phase with (1) the low level circulation on the western side of South America, where a ridge over a high-pressure system is located and (2) a relative upper low pressure lying over the low-pressure system at the SE of South America (Figures 9b–9d).

3.4.2. Wave Parameters

[19] The flow at 600 hPa from SE over the Antarctic Peninsula generates intense MWs in SE-NW direction (solid line in Figure 9a), with peak-to-peak *w* amplitudes around 5 m/s at 600 hPa to decrease abruptly above 100 hPa (Figures 9b–9d, 10a, and 10b). A predominant λ_H around 20 km is observed (Figure 10c). λ_z was estimated between 2 and 4 km (this last at 250 hPa). U_H ranges between 30 m/s at 600 hPa to suddenly rotate into SW-NE direction, above 100 hPa. The wave seems to encounter a critical layer here. τ for this mode varies between 45 and 125 min. λ_z (τ) is maximum (minimum) around 250 hPa.

3.5. Case 5 (19 July, 71°S)

3.5.1. Synoptic Circulation

[20] The Atlantic Subtropical anticyclone is positioned over the continental zone, with its southern flank over the Drake Passage, yielding a strong low level flow from the west at all tropospheric levels (Figures 11a–11d). At the upper levels, a similar configuration with a strong ridge at 200 hPa is present.

3.5.2. Wave Parameters

[21] A more complex MWs distribution is observed in this region (Figures 11b–11d). Two dominant MW modes (solid line in Figure 11a) with λ_h between 30–40 and 70 km (*w* CWT at 600 hPa) and a considerable variation in λ_z between 2 and 10 km, because of the strongly variable background shear, are observed (Figures 12c and 12a). U_H

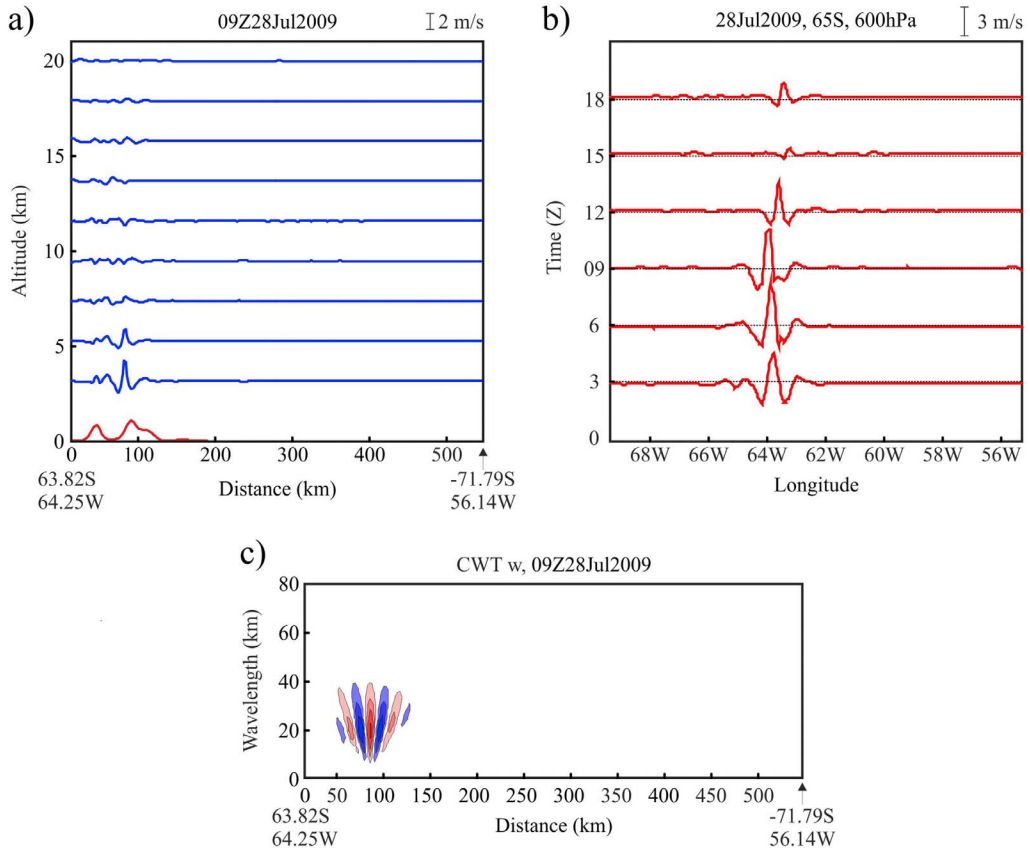

Figure 10. Case 4: w as a function of (a) altitude along the perpendicular direction to the dominant wave crests shown in Figure 9a and (b) time along the proposed racetrack direction (Figure 9a). (c) The w CWT at 600 hPa along the same direction as in Figure 10a.

ranges between 15 and 35 m/s (this last at 200 hPa); τ for these modes vary between 16 and 140 min. λ_z (τ) is maximum (minimum) around 250 hPa. The w peak-to-peak amplitudes reach maximum values near 5 m/s at lower levels (600 hPa) and decrease continuously with height.

4. Vertical Flux of Momentum and Energy Equipartition

[22] We discuss now the zonal and meridional components of the vertical flux of horizontal momentum (M_x and M_y, respectively) computed from the above simulations. The topographic height as well as the ground pressure distribution are considerably asymmetric in the zonal direction. M_x and M_y may be defined as integrations along a chosen path. As pointed out by *Smith et al.* [2008], this path may be neither necessarily perpendicular to the wave phase lines nor parallel to the mean wind. We perform the integration below, along constant latitude paths (R):

$$M_{xR} = \bar{\rho}_0 \int_R uwdx \tag{2}$$

$$M_{yR} = \bar{\rho}_0 \int_R vwdx \tag{3}$$

where $\bar{\rho}_0$ is the mean density along R. u and v represent the zonal and meridional wave perturbations already band pass filtered between 12 and 400 km (as in the case of w, for simplicity we omit the usual prime notation here and subindexes $_{bp}$). Following *Smith et al.* [2008], these quantities should be independent of the length R if this is long enough to contain all the large waves. This assertion has been tested and verified in each of the cases, by trying several path lengths, to the West well above the Pacific Ocean (considering a wider domain than in Figure 1) and to the East above the landscapes and the Atlantic Ocean. All paths tested in all cases contained the largest wave amplitudes above the mountains. According to *Eliassen and Palm* [1961], M_{xR} and M_{yR} are independent of altitude in steady nondissipative flow, even in the presence of background shear and lapse rate variations. Nevertheless, Coriolis acceleration effects in long waves (exceeding O(100 km)), as well as slow time mean flow variations, may violate this. In addition, because of the computation of momentum flux along a line instead of over an area, three-dimensional effects could also cause apparent violations of the Eliassen-Palm theorem.

[23] In each case, M_{xR}, M_{yR} and the magnitude of the momentum flux $M_R = (M_{xR}^2 + M_{xR}^2)^{0.5}$ were calculated at constant pressure levels every 50 hPa between 600 and 50 hPa and constant latitude paths (Figure 13). This last selection was made with the additional purpose of examining how fluxes that might be picked up by an aircraft along different segments, to allow comparison with the above mentioned planned SAANGRIA Experiment. We did not consider levels below 600 hPa. As in section 3, we

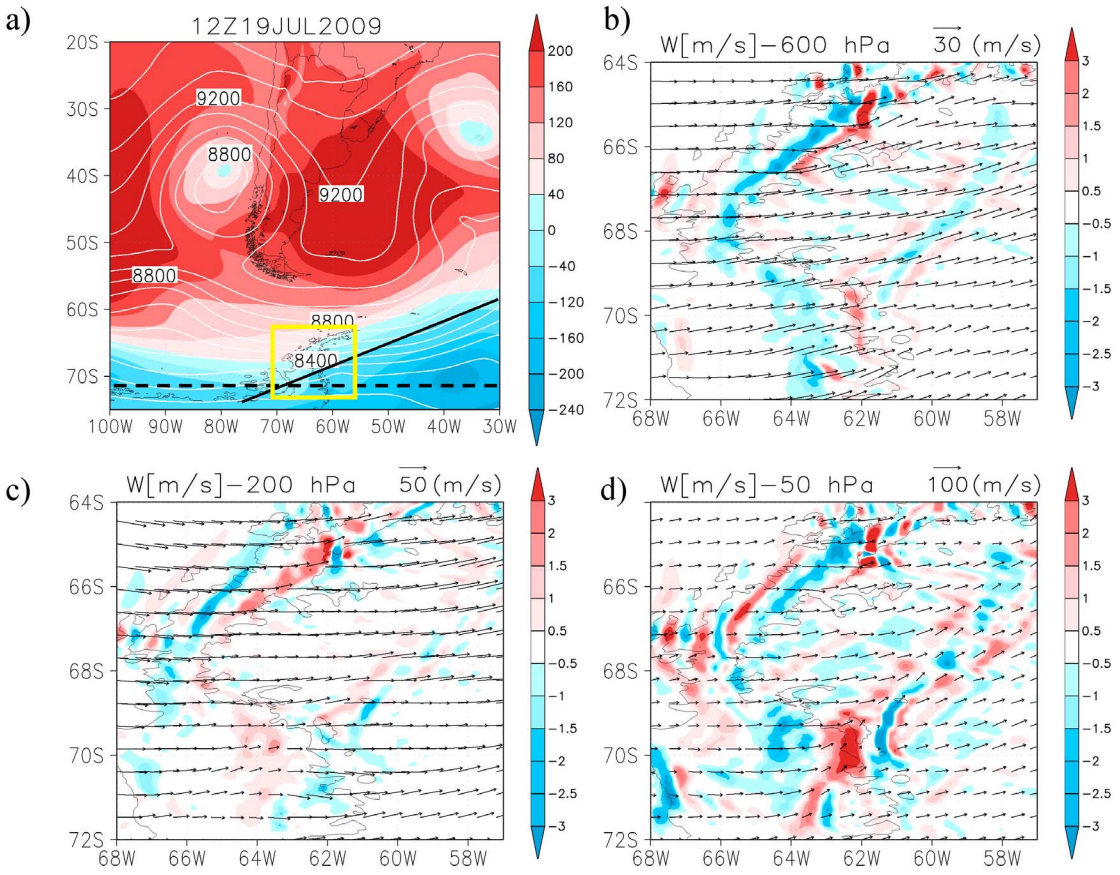

Figure 11. The same as Figure 3, but for case 5.

considered u, v and w to be band pass filtered. These cutoffs include a sufficiently broad spectrum of the representative MWs in the region. An additional calculation (not shown in Figure 13) was performed, with narrower cutoff intervals around the prevailing λ_H in each case, revealed by the corresponding w CWTs. This was intended to isolate the contribution by the prevailing wave from the rest of the spectrum. According with a previous theoretical prediction [see, e.g., *Ern et al.*, 2004] the proportionality of the momentum flux vector associated to the prevailing mode to the ratio $\mathbf{k}_H/k_v$, was verified.

[24] In cases 1–5, we see the following general and particular features (Figure 13).

[25] 1. Prevailing M_{xR} and M_R values at higher pressure levels that decrease with increasing height are clearly observed. After a considerable deposition of momentum with progressive levels, the flux is reduced to relatively negligible values at the upper heights here considered. A prevailing negative zonal component is observed almost everywhere, with the exception of case 4. This last is explained by the relative orientation of the mean wind to the Antarctic Peninsula. In the remaining cases, the vast majority of GWs against the mean eastward flow is a characteristic in the wintertime stratosphere. In general, the fluxes were detected to be mostly westward, but significantly meridional values also occurred.

[26] 2. Case 1 represents an extreme situation which overcomes by a factor of 10 the largest fluxes computed in the remaining cases. This is associated with the prevailing wind intensity and direction, the mountain range alignment at 49°S, the large amplitudes in w (Figures 3b–3d and 4a), and those corresponding to u and v (not shown).

[27] 3. In case 3, the proposed generation of traveling GWs at low levels by a possible shear source over the Drake Passage is in agreement with a sudden interruption due to overturning and wave breaking at a layer around 300 hPa, with a substantial deposition of momentum there.

[28] The progressive deposition of momentum at increasing heights from lower to upper levels, which is clearly reflected in Figures 13a and 13e, may be explained as follows. As mentioned before, in addition to possible local wave breaking, critical level and partial reflection effects, three-dimensional effects may cause departures from the Eliassen-Palm prediction. Nevertheless, nonsteadiness in the background flow should be considered too. In a more simplified scenario, *Chen et al.* [2005] showed how significant vertical gradients in momentum flux can be produced by very slowly varying large-scale flows (time scale around 2 days). These authors considered the evolution of mountain-wave-induced momentum flux through idealized numerical simulations, during the passage of a time-evolving synoptic-scale flow over an isolated 3D mountain, high enough, to preserve a moderate degree of nonlinearity. If we observe the evolution of the background wind during the 24 h preceding the situation exhibited at 600 hPa in Figure 3b (not shown), a progressive clockwise rotation of 35° with a constant intensity around 30 m/s takes place. It remains to understand the relative importance of these (and possibly

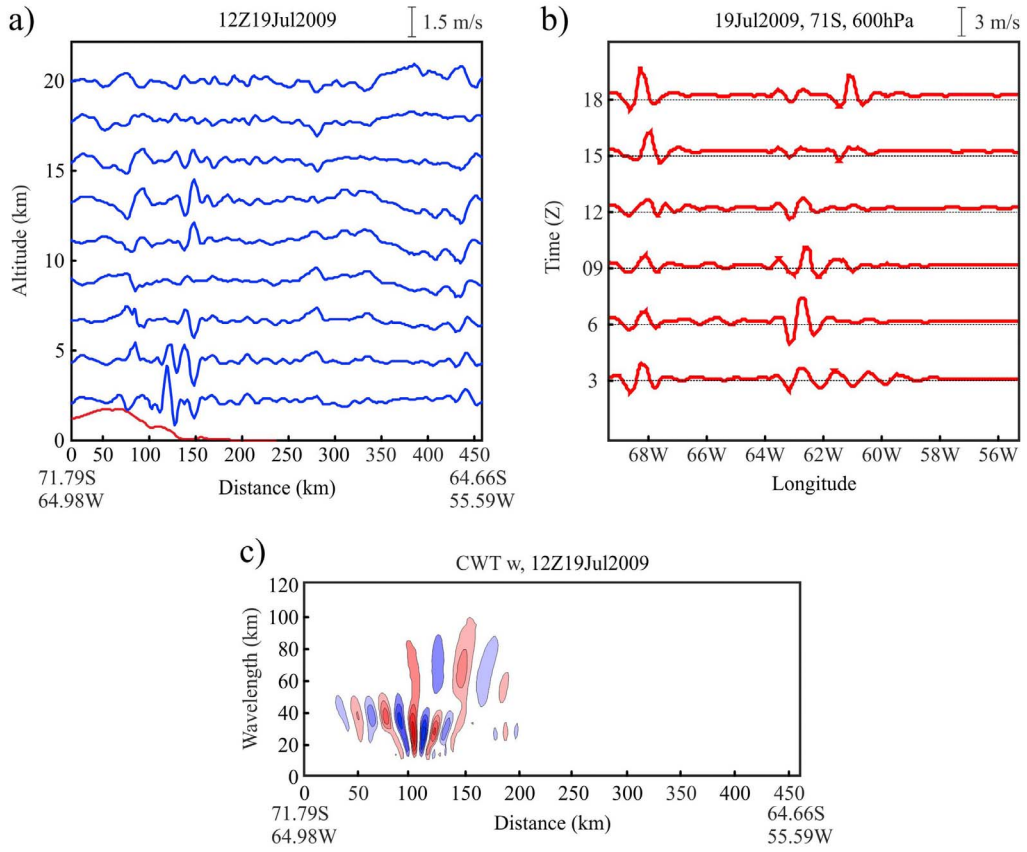

Figure 12. Case 5: w as a function of (a) altitude along the perpendicular direction to the dominant wave crests shown in Figure 10a and (b) time along the proposed racetrack direction (Figure 10a). (c) The w CWT at 600 hPa along the same direction as in Figure 12a.

additional) processes, in the momentum deposition at different heights.

[29] A comparison can be made with previous experimental studies mentioned in section 1. We must first standardize both procedures: The specific average chosen by other authors, computed the flux of momentum density per unit time and unit area. This may be expressed in pressure units. As mentioned above, from (2) and (3) we know that the integration along any horizontal coordinate crossing the mountains allows to obtain $\mathbf{M}_R$ zonal and meridional components that do not depend on the integration path length [e.g., *Smith et al.*, 2008]. Following this, we note that the momentum flux results in Figure 13 are presented in pressure times distance units, corresponding to the flux of momentum density per unit time and unit longitude (instead of per unit time and unit area). Now, if we divide our M_{xR} results corresponding to a given region and altitude by a zonal segment Δx, where $[\Delta x, \Delta y]$ represents the [zonal, meridional] region where the zonal momentum flux chosen by other authors was averaged, both results should may be comparable. For example, $\Delta x \sim 720$ km at 71°S, according to the Vorcore results reported by *Vincent et al.* [2007] in longitude by latitude cells of 20° × 5°. At 71°S, between 50 and 100 hPa, we obtained −5.6 KN/m. Dividing by 720 km, we obtain -0.78×10^{-5} KN m^{-2} = −7.8 mPa. This value is comparable to the mean values of −3.4 mPa obtained by *Vincent et al.* [2007], taking into account that these authors also found the zonal momentum flux to be negative almost everywhere during the wintertime stratosphere and locally reached −12 mPa over the Antarctic Peninsula.

[30] A second comparison can be made with satellite (HIRDLS) T vertical profiles and the procedure followed by *Ern et al.* [2004]. As mentioned in section 1, *Alexander et al.* [2008] obtained estimates of momentum flux in the southern Andes Range, averaged between 20 and 30 km height and 30 days during May 2006, reporting values of 5 mPa and using 5° latitude by 30° longitude bins. In this region, our results (Figure 13) corresponding to case 1 in the lower stratosphere, in pressure units, after considering the average over the 30° longitude bin applied by *Alexander et al.* [2008], indicate values of 10–20 mPa between 50 and 100 hPa. In this comparison we must take into account important constraints; in particular, the method from Ern et al. tends to underestimate momentum fluxes, as it considers that one dominant monochromatic wave in the hydrostatic approximation, carries the momentum flux. MWs near to Andes and in particular in case 1, are essentially nonhydrostatic.

[31] To identify possible partial wave reflection effects near the tropopause, we computed the equipartition ratio between potential and kinetic wave energy densities

$$\mathrm{EQR} = \frac{\mathrm{PE}}{\mathrm{KE}} = \frac{(1/2)\bar{\rho}_0 (g^2/N^2) \int_R \left(\frac{T'}{\bar{T}}\right)^2 dx}{(1/2)\bar{\rho}_0 \int_R (u^2 + v^2 + w^2) dx} \qquad (4)$$

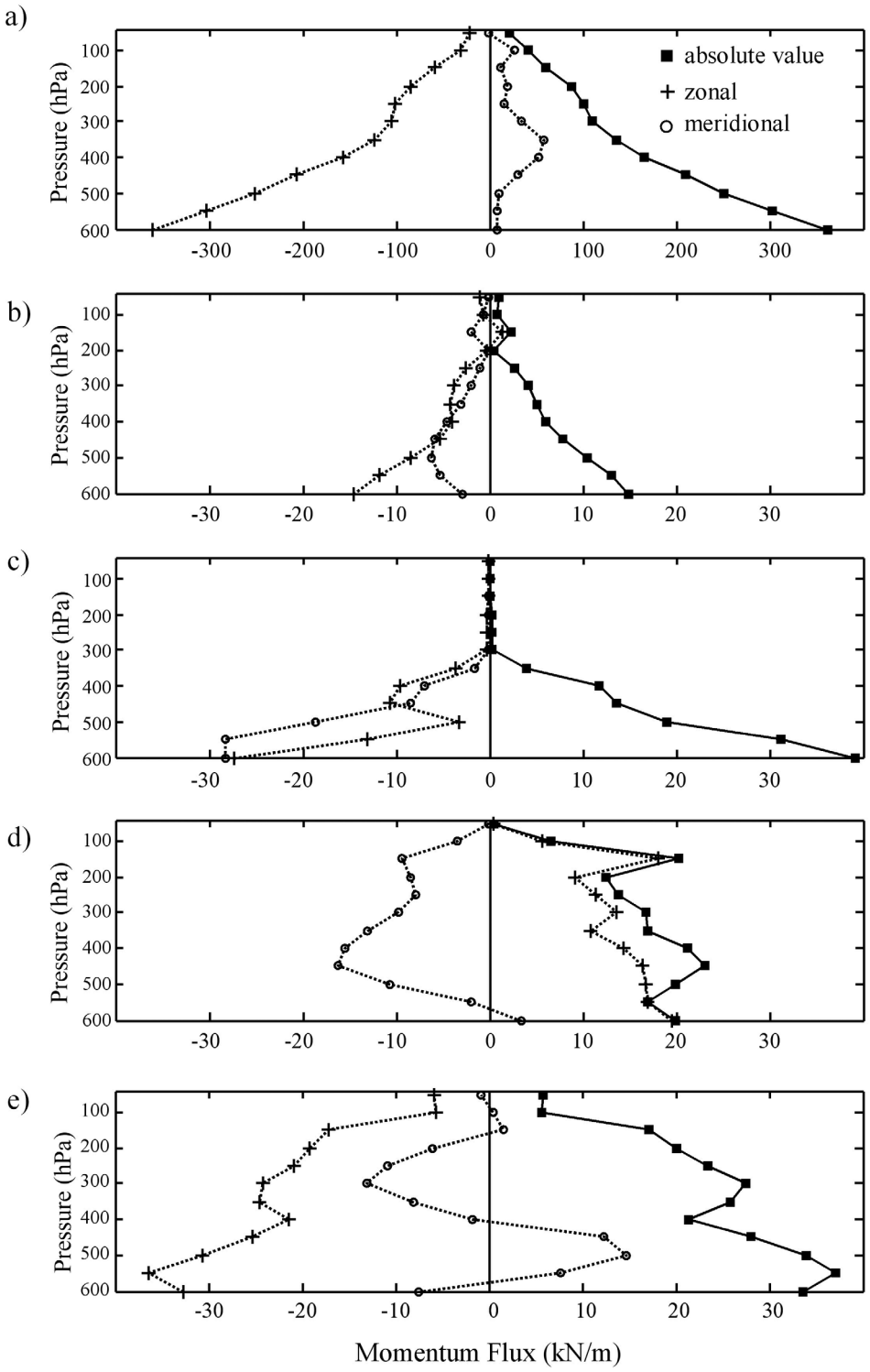

Figure 13. M_{xR} (crosses), M_{yR} (circles), and the magnitude of the momentum flux (absolute value) $M_R = (M_{xR}^2 + M_{xR}^2)^{0.5}$ (squares) at constant pressure levels every 50 hPa between 600 and 50 hPa and constant latitude paths for cases (a) 1, (b) 2, (c) 3, (d) 4, and (e) 5.

where g is the acceleration of gravity. EQR is expected to depart from unity whenever both upgoing and downgoing waves are present at a given level. In the five cases and at every pressure level, EQR is always less than one and exhibits a considerable variability (Table 1). We may differentiate between two situations: In cases 1 and 2, maximum values of EQR may be found at lower and upper pressure levels, while around the tropopause, roughly situated around 200 hPa, this ratio is minimized. On the other hand, the behavior of EQR in cases 3, 4, and 5 is clearly the

Table 1. Potential/Kinetic Wave Energy Density Ratio

Pressure Level (hPa)	Case 1	Case 2	Case 3	Case 4	Case 5
6.00E + 2	3.53E-1	6.92E-1	2.79E-2	2.09E-1	2.29E-2
5.50E + 2	3.06E-1	2.16E-1	1.56E-2	8.02E-2	2.84E-2
5.00E + 2	3.13E-1	1.53E-1	1.09E-2	2.13E-2	4.50E-2
4.50E + 2	2.87E-1	2.00E-1	1.02E-2	8.72E-3	6.27E-2
4.00E + 2	1.58E-1	3.28E-1	3.40E-2	1.78E-2	1.33E-1
3.50E + 2	4.84E-2	2.67E-1	7.34E-2	7.19E-2	2.40E-1
3.00E + 2	4.45E-2	1.02E-1	3.03E-1	1.80E-1	3.22E-1
2.50E + 2	1.98E-1	1.83E-1	3.49E-1	1.87E-1	2.00E-1
2.00E + 2	1.93E-1	1.62E-1	4.75E-1	1.48E-1	1.02E-1
1.50E + 2	1.85E-1	1.46E-1	3.23E-1	1.85E-1	1.22E-1
1.00E + 2	7.84E-1	2.29E-1	1.49E-1	2.52E-1	8.85E-2
5.00E + 1	4.29E-1	2.87E-1	1.49E-1	8.14E-2	8.67E-2

opposite. In general, strong EQR variations may be considered as an indication of partial reflection [e.g., *Smith et al.*, 2008]. Our results do not seem to correspond to a scenario with only pure upward or pure downward waves, where EQR would be expected to be closer to one. In the cases above considered, in addition to a partial identification of reflection, breaking and critical layering processes, we are still uncertain about additional effects, as nonlinear generation of trapped waves and downgoing waves generated in the stratosphere.

5. Conclusions

[32] The five case studies considered along the southern Andes range, the Drake Passage, and its prolongation in the Antarctic Peninsula revealed the following features.

[33] Above continental regions, systematic large-amplitude, stationary, nonhydrostatic GW wave structures, forced by the mountains up to the lower stratosphere and persisting during several hours are observed. Over the Drake Passage, one large-amplitude propagating wave structure was identified during the 3 month period considered but MWs were not identified.

[34] The *w* CWT analysis at uniform pressure levels perpendicularly to the nominal orientation of the dominant wave crests, was adequate for these MW simulations.

[35] One or, at the most, two prevailing modes of oscillation, were clearly identified in each case.

[36] In all cases, the dominant modes were characterized by horizontal wavelengths around 50 km. Their vertical wavelengths, were strongly variable because of a usually permanent intense background wind and were estimated to be between 2 and 11 km. The corresponding intrinsic periods ranged in a broad spectrum usually between 10 min and less than 1 h, but sometimes peaking near 2 h. In general, the estimated vertical wavelength and intrinsic periods reached extreme values around 250–300 hPa.

[37] The synoptic circulation during each of the five cases considered, exhibited different cyclonic-anticyclonic circulation at low levels, as well as geopotential distributions at high levels. During the 3 month period considered in the simulations, 97 synoptic hours were affected by a low-pressure system in the region; nevertheless, this period was not sufficient to draw general conclusions linking synoptic conditions with MWs generation.

[38] An analysis of the zonal and meridional components of the vertical flux of horizontal momentum for these cases, included horizontal wavelength harmonics between 12 and 400 km. Large flux values at higher pressure levels, decreasing with increasing height was observed, after a progressive deposition of momentum. Partial reflection, breaking and critical layering processes were identified. As expected in the wintertime upper troposphere and lower stratosphere in this region, a prevailing zonal component is observed negative almost everywhere, with the exception of one case above the Northern tip of the Antarctic Peninsula. A comparison with previous experimental results reported in the region from in situ (long duration balloons) and remote sensing (satellite data) measurements, putting special attention in the space averaging used by other authors, suggests a good agreement with the flux profiles here reported from our simulations.

[39] Partial wave reflection produced considerable departures from equipartition between potential and kinetic wave energy in all cases and at all pressure levels. This ratio was always less than one below the lower stratosphere.

[40] The frequent generation of large-amplitude MWs in the region during the 3 months analyzed suggest that the five constant latitude racetracks proposed for the SAANGRIA experiment intersect the mountain tops where an almost permanent generation of intense MWs takes place. Nevertheless, because of (1) the rapid deposition of momentum at progressive pressure levels, (2) the fluctuating departures from the wave energy equipartition hypothesis, and (3) the dominant orientation of wave crests, we make the following suggestion for the operational design of a field experiment as SAANGRIA: the inclusion also of some aircraft flights at several altitudes, from middle troposphere to lower stratosphere, perpendicularly directed along the expected dominant wave number vectors, may optimize the information on MWs generation, propagation and dissipation obtained in the region.

[41] **Acknowledgments.** This paper was prepared under grants UBA X004, CONICET PIP 5932, and ANPCyT PICT 1999. A. de la Torre and P. Alexander are members of and P. Llamedo holds a fellowship from CONICET. The GFZ contribution was partially funded through DFG priority program CAWSES SPP 1176. We acknowledge data provided by the NOAA CIRES/Climate Diagnostics Center, Boulder (Colorado) from their Web site http://www.cdc.noaa.gov. The authors thank the ECMWF for providing the ERA-Interim data.

References

Alexander, M. J., and H. Teitelbaum (2007), Observation and analysis of a large amplitude mountain wave event over the Antarctic peninsula, *J. Geophys. Res.*, *112*, D21103, doi:10.1029/2006JD008368.

Alexander, M. J., et al. (2008), Global estimates of gravity wave momentum flux from High Resolution Dynamics Limb Sounder observations, *J. Geophys. Res.*, *113*, D15S18, doi:10.1029/2007JD008807.

Alexander, M. J., S. D. Eckermann, D. Broutman, and J. Ma (2009), Momentum flux estimates for South Georgia Island mountain waves in the stratosphere observed via satellite, *Geophys. Res. Lett.*, *36*, L12816, doi:10.1029/2009GL038587.

Boccara, G., A. Hertzog, R. A. Vincent, and F. Vial (2008), Estimation of gravity wave momentum flux and phase speeds from quasi-Lagrangian stratospheric balloon flights. Part I: Theory and simulations, *J. Atmos. Sci.*, *65*(10), 3042–3055.

Chen, C.-C., D. R. Durran, and G. J. Hakim (2005), Mountain-wave momentum flux in an evolving synoptic-scale flow, *J. Atmos. Sci.*, *62*(9), 3213–3231.

de la Torre, A., P. Alexander, P. Llamedo, C. Menéndez, T. Schmidt, and J. Wickert (2006), Gravity waves above the Andes detected from GPS radio occultation temperature profiles: Jet mechanism?, *Geophys. Res. Lett.*, *33*, L24810, doi:10.1029/2006GL027343.

Eliassen, A., and E. Palm (1961), On the transfer of energy in stationary mountain waves, *Geofys. Publ.*, *22*, 1–23.
Ern, M., P. Preusse, M. J. Alexander, and C. D. Warner (2004), Absolute values of gravity wave momentum flux derived from satellite data, *J. Geophys. Res.*, *109*, D20103, doi:10.1029/2004JD004752.
Fritts, D. C., and M. J. Alexander (2003), Gravity wave dynamics and effects in the middle atmosphere, *Rev. Geophys.*, *41*(1), 1003, doi:10.1029/2001RG000106.
Fritts, D. C., R. B. Smith, J. D. Doyle, and S. Eckermann (2010), Overview of the Southern Andes—Antarctic Gravity wave Initiative (SAANGRIA), paper presented at 14th Conference on Mountain Meteorology, Am. Meteorol. Soc., Olympic Valley, Calif.
Gill, A. E. (1982), *Atmosphere-Ocean Dynamics*, 662 pp., Academic, New York.
Hamming, R. W. (1998), *Digital Filters*, 3rd ed., Dover, Mineola, N. Y.
Hertzog, A., G. Boccara, R. A. Vincent, F. Vial, and P. Cocquerez (2008), Estimation of gravity wave momentum flux and phase speeds from quasi-Lagrangian stratospheric balloon flights. Part II: Results from the Vorcore campaign in Antarctica, *J. Atmos. Sci.*, *65*(10), 3056–3070.
Plougonven, R., A. Hertzog, and H. Teitelbaum (2008), Observations and simulations of a large-amplitude mountain wave breaking over the Antarctic Peninsula, *J. Geophys. Res.*, *113*, D16113, doi:10.1029/2007JD009739.
Preusse, P., S. D. Eckermann, and M. Ern (2008), Transparency of the atmosphere to short horizontal wavelength gravity waves, *J. Geophys. Res.*, *113*, D24104, doi:10.1029/2007JD009682.
Shutts, G. J., and S. B. Vosper (2011), Stratospheric gravity waves revealed in NWP model forecasts, *Q. J. R. Meteorol. Soc.*, *137*(655), 303–317.
Shutts, G. J., M. Kitchen, and P. H. Hoare (1988), A large amplitude gravity wave in the lower stratosphere detected by radiosonde, *Q. J. R. Meteorol. Soc.*, *114*, 579–594.
Simmons, A. J., et al. (2007), ERA-Interim: New ECMWF reanalysis products from 1989 onwards, *ECMWF Newsl.*, *110*, 25–35.
Skamarock, W. C., J. B. Klemp, J. Dudhia, D. O. Gill, D. M. Barker, M. Duda, X.-Y. Huang, W. Wang, and J. G. Powers (2008), A description of the advanced research WRF version 3, *Tech. Note NCAR/TN-475+STR*, Natl. Cent. for Atmos. Res., Boulder, Colo.
Smith, R. B. (1979), The influence of mountains on the atmosphere, *Adv. Geophys.*, *21*, 87–230.
Smith, R. B., B. K. Woods, J. Jensen, W. A. Cooper, J. D. Doyle, Q. Jiang, and V. Grubii (2008), Mountain waves entering the stratosphere, *J. Atmos. Sci.*, *65*, 2543–2562.
Vincent, R. A., and I. M. Reid (1983), HF Doppler measurements of mesospheric momentum fluxes, *J. Atmos. Sci.*, *40*, 1321–1333.
Vincent, R. A., A. Hertzog, G. Boccara, and F. Vial (2007), Quasi-Lagrangian superpressure balloon measurements of gravity-wave momentum fluxes in the polar stratosphere of both hemispheres, *Geophys. Res. Lett.*, *34*, L19804, doi:10.1029/2007GL031072.
von Storch, H., H. Langenberg, and F. Feser (2000), A spectral nudging technique for dynamical downscaling purposes, *Mon. Weather Rev.*, *128*, 3664–3673.
Wang, L., and M. J. Alexander (2010), Global estimates of gravity wave parameters from GPS radio occultation temperature data, *J. Geophys. Res.*, *115*, D21122, doi:10.1029/2010JD013860.
Wu, D. L., P. Preusse, S. D. Eckermann, J. H. Jiang, M. de la Torre Juarez, L. Coy, B. Lawrence, and D. Y. Wang (2006), Remote sounding of atmospheric gravity waves with satellite limb and nadir techniques, *Adv. Space Res.*, *37*, 2269–2277.

P. Alexander, Departamento de Física, Facultad de Ciencias Exactas y Naturales, Universidad de Buenos Aires, Ciudad Universitaria, 1428 Buenos Aires, Argentina. (peter@df.uba.ar)

A. de la Torre, R. Hierro, P. Llamedo, and A. Rolla, Facultad de Ingeniería, Universidad Austral, Avda. Garay 125, 5to Piso, C1063ABB Buenos Aires, Argentina. (adelatorre@austral.edu.ar; rhierro@austral.edu.ar; pllamedo@austral.edu.ar; arolla@austral.edu.ar)

T. Schmidt and J. Wickert, Helmholtz Centre Potsdam, GFZ German Research Centre for Geosciences, Telegrafenberg A17, D-14473 Potsdam, Germany. (tschmidt@gfz-potsdam.de; wickert@gfz-potsdam.de)